




Multiple robust Dirac states in hexagonal lattice induced by p - d electron-counting rule and bilayer stacking

Bingwen Zhang ^{1,2,*}, Jie Sun ³, Jiancai Leng ³, Cheng Zhang,¹ Huamin Chen ¹ and Jun Wang ^{1,†}

¹*Fujian Key Laboratory of Functional Marine Sensing Materials, Center for Advanced Marine Materials and Smart Sensors, Minjiang University, Fuzhou 350108, People's Republic of China*

²*Beijing National Laboratory for Condensed Matter Physics, Institute of Physics, Chinese Academy of Sciences, Beijing 100190, People's Republic of China*

³*School of Electronic and Information Engineering, Department of Physics, Qilu University of Technology, Shandong Academy of Sciences, Jinan 250353, Shandong, People's Republic of China*



(Received 9 July 2020; revised 23 August 2020; accepted 15 September 2020; published 6 October 2020)

In this paper, we predict two-dimensional transition metal boride TiB_2C_2 and HfB_2C_2 nanosheets, which exhibit favorable mechanical and thermal properties. Young's moduli of TiB_2C_2 and HfB_2C_2 are 137.8 and 128.9 N/m, respectively. Both nanosheets could sustain up to 500 K based on our *ab initio* molecular dynamics results. In addition, both nanosheets are semimetallic, exhibiting 12 Dirac cones in the first Brillouin zone, six pairs of which form compensated electron-hole pockets. Under different types of external strains, both TiB_2C_2 and HfB_2C_2 are robust, and the Dirac cones could be tuned to be anisotropic. We propose that the multiple Dirac cones are induced by a combination of the p - d electron-counting rule and bilayer stacking; to verify our opinion, we also predicted and proved that TB_2Si_2 ($T = \text{Ti, Zr, Hf}$) are mechanical stable two-dimensional nanosheets with multiple Dirac cones based on phonon and electronic band structure calculations.

DOI: [10.1103/PhysRevB.102.165404](https://doi.org/10.1103/PhysRevB.102.165404)

I. INTRODUCTION

Since the discovery of graphene [1], Dirac fermions have attracted great interest, especially in the two-dimensional (2D) hexagonal lattice. Dirac fermions, which emerge in the Brillouin zone (BZ) as a linear cross point between the valence band and conduction band, possess some extraordinary properties such as high electron mobility and low-power dissipation, and they are very promising for next-generation electronics. Experiments have confirmed some hexagonal Dirac materials in group IV 2D materials such as graphene [1], silicene [2], germanene [3], stanene [4], etc. The hexagonal lattice is prone to exhibit Dirac states for its symmetry associated with some covalent bond property.

Inspired by the discovery of graphene, which is stabilized by sp^2 and three-coordinate bond character (each atom has s^2p^2 valence electrons), it is rational to speculate that a neighbor group such as boron could form stable 2D Dirac materials with one missing electron supplemented. Following this idea, one could stabilize the hexagonal lattice by the introduction of additional boron atoms into the honeycomb lattice to balance out the two- and multicenter bonds [5–7]. And this rule provides great opportunities in this field because additional boron atoms could be introduced in the honeycomb lattice with a lot of different arrangements [6–8].

In addition, transition metals (TMs) with additional d electrons are also promising alternatives to form stable a TM boride hexagonal lattice. TiB_2 [9] was the first predicted stable 2D Dirac TM boride hexagonal lattice, which extended

the Dirac materials to metal diborides; each Ti atom stands above the center of the honeycomb lattice. This strategy was also extensively followed to predict stable 2D ZrB_2 [10,11], HfB_2 [12], FeB_2 [13], and FeB_6 [14], all of which possess Dirac states. In addition, with both metal and boron atoms introduced in the honeycomb lattice, CuB_3 , CuB_6 , and Cu_7B_{15} are also predicted to be stable nanosheets, and the Cu_7B_{15} nanosheet exhibits a Dirac nodal line in the BZ [15].

It is interesting that the bilayer boron honeycomb lattice with an appropriate TM sandwiched between the layers could also be stable 2D Dirac materials, such as CrB_4 [16], MoB_4 [17], WB_4 [18], and UB_4 [19] nanosheets. The Dirac states and stability are predictable considering that Cr atoms could offer the $3d^4$ electrons to the four boron atoms. Compared with TB_2 nanosheets, the TB_4 nanosheets could exhibit multiple Dirac states along the Γ - M - K - Γ high-symmetry line in the BZ.

In addition to theoretical investigations, 2D TM borides have also been investigated and successfully synthesized in experimental research. Cepek *et al.* [20] synthesized MgB_2 thin films in ultrahigh-vacuum conditions via molecular beam epitaxy (MBE), and this research provided the possibility of controlled doping of MgB_2 . TiB_2 sheets synthesized at the interface of TiC and B_4C also have been reported [21]. Rich AlB_2 -type bulk structures (ScB_2 , TiB_2 , VB_2 , CrB_2 , ZrB_2 , NbB_2 , MoB_2 , TaB_2 , HfB_2 , YB_2 , etc.) [22–27] offer great opportunities to 2D TM borides. In addition, 2D MoB was also successfully synthesized by etching the Al atoms from MAB phase (where M, A, and B are metal, aluminum, and boron atoms, respectively) Mo_2AlB_2 [28]; this method is similar to that of synthesizing MXene from MAXenes [29,30].

*turney0524@163.com

†wjnaf@163.com

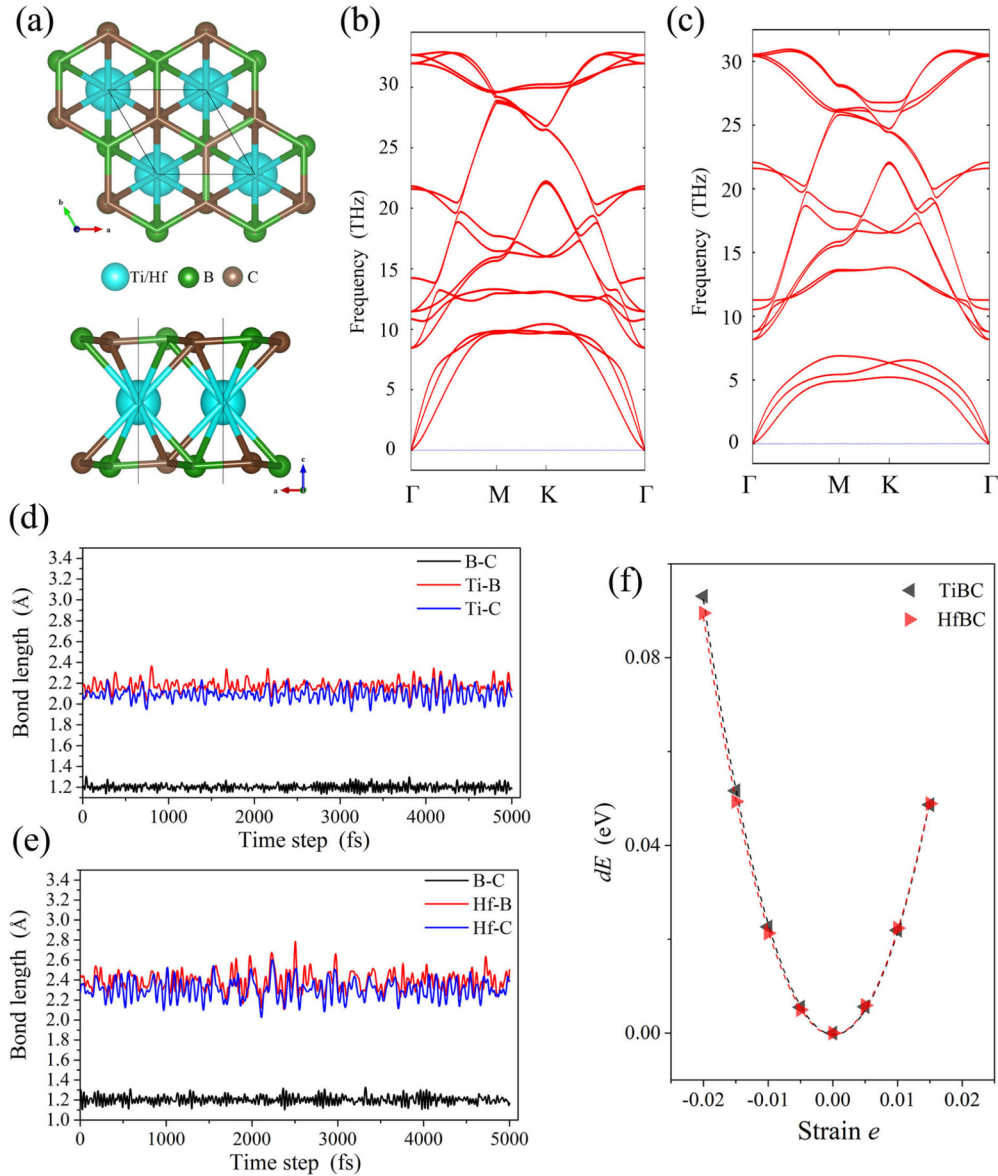


FIG. 1. (a) The geometric structures, (b) and (c) phonon dispersion, (d) and (e) AIMD results at 500 K of bond-length variations, and (f) in-plane isotropic biaxial strain and energy curve of TiB₂C₂ and HfB₂C₂ nanosheets, respectively.

To further explore and extend the 2D Dirac state TM boride nanosheet family, in this paper, we find that TiB₂C₂ and HfB₂C₂ nanosheets are also stable nanosheets, and both of them exhibit six pairs of Dirac cones which form compensated electron-hole pockets in the first BZ. The Dirac states are both robust with the absence of spin-orbit coupling (SOC) against different types of external strains. In combination with density function theory (DFT) and the tight-binding model, we propose a mechanism in which multiple robust Dirac states in a hexagonal lattice are induced by the combination of the *p-d* electron-counting rule and bilayer stacking. We further verify this mechanism with successful prediction of stable multiple Dirac state hexagonal lattice TiB₂Si₂, ZrB₂Si₂, and HfB₂Si₂ nanosheets. The mechanism is very promising for exploring 2D Dirac state materials.

II. COMPUTATIONAL DETAILS

Our calculations are based on the DFT method to carry out the analysis of the structural stabilities and the electronic structures. Numerical calculations are performed by plane-wave-based DFT within the generalized gradient approximation [31], and the exchange-correlation potential of the Perdew-Burke-Ernzerhof functional is used as implemented in the Vienna Ab initio Simulation Package (VASP) [32]. The projector augmented wave potentials explicitly include three valence electrons for B ($2s^2 2p^1$) and four for Ti ($3d^2 4s^2$) and Hf ($5d^2 6s^2$). The phonon band structures of the corresponding crystal structures are computed by the PHONOPY package [33], which is integrated with the density functional perturbation theory [34]. To validate the thermal stability of the nanosheets, *ab initio* molecular dynamics

TABLE I. Structure parameters (Å) and mechanical properties (N/m) of TiB_2C_2 and HfB_2C_2 nanosheets.

| | Lattice | TM-B | TM-C | B-C | Thickness | Y_{2D} |
|--------------------------|---------|-------|-------|-------|-----------|----------|
| TiB_2C_2 | 2.758 | 2.400 | 2.333 | 1.595 | 3.501 | 137.8 |
| HfB_2C_2 | 2.823 | 2.542 | 2.472 | 1.633 | 3.809 | 128.9 |

(AIMD) simulations lasting for 5 ps with a time step of 1.0 fs are performed. The AIMD simulations were in the NVT ensemble, and the temperature was controlled by using the Nosé-Hoover method [35].

In this paper, we take a large plane-wave cutoff of 600 eV and set the energy convergence criterion to be 10^{-6} eV. A Γ -centered $21 \times 21 \times 1$ Monkhorst-Pack k -point mesh is used for the Brillouin-zone integrations in the nanosheets [36]. The total energies are calculated using the linear tetrahedron method with Bloch corrections [37]. During structural relaxation, atomic positions are relaxed until the Hellman-Feynman forces are less than 10^{-3} eV/Å.

III. RESULT AND DISCUSSION

A. Geometric structure and stability of TiB_2C_2 and HfB_2C_2 nanosheets

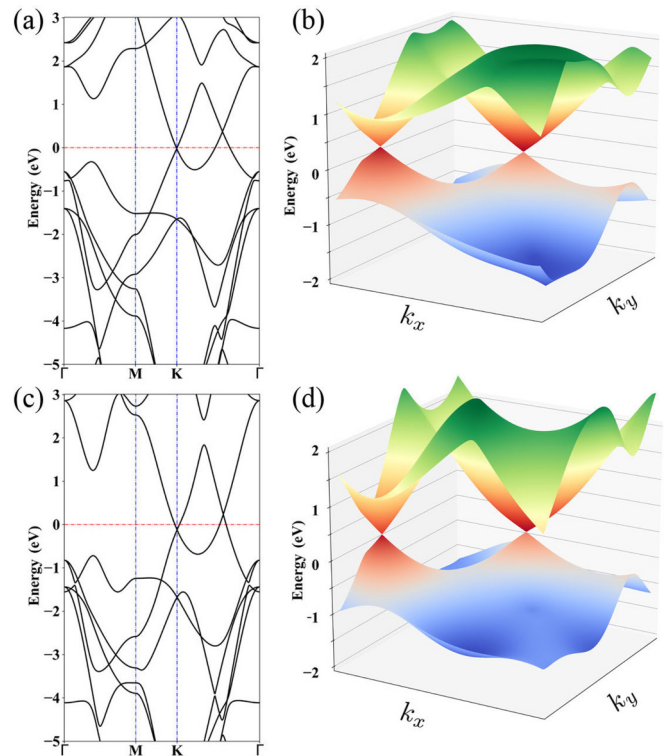
As shown in Fig. 1(a), the symmetry of the optimized geometric structure of the TiB_2C_2 and HfB_2C_2 nanosheets is D_{3d} , and the lattice parameters are 2.758 and 2.823 Å for TiB_2C_2 and HfB_2C_2 , respectively. They both consist of one layer of Ti or Hf atoms sandwiched by two layers of graphenelike hexagonal B-C atoms rather than C-C atoms. The thicknesses of TiB_2C_2 and HfB_2C_2 nanosheets are 3.501 and 3.809 Å, respectively. Detailed structure properties are shown in Table I.

We further confirmed the stability of the two nanosheets with the calculations of cohesive energy, AIMD, and phonon band structures. The cohesive energy per atom $E_{\text{coh}} = (E_{TM} + 2E_B + 2E_C - E_{TM\text{B}_2\text{C}_2})/5$, where E_{TM} , E_B , E_C , and $E_{TM\text{B}_2\text{C}_2}$ are the total energies per Ti or Hf atom, per B atom, per C atom, and per TB_2C_2 formula unit, respectively. The cohesive energies are 6.33 and 6.76 eV per atom for the TiB_2C_2 and HfB_2C_2 nanosheets, respectively. The results are larger than those of the FeB_2 (4.87 eV) and FeB_6 (5.79 eV) nanosheets [13,14].

We calculated the phonon dispersion relations of both nanosheets; the results are presented in Figs. 1(b) and 1(c), which suggest that they are both mechanically stable in the absence of imaginary frequencies in the phonon band structures.

To further confirm the thermal stability of both nanosheets, we performed an AIMD simulation with a $5 \times 5 \times 1$ supercell of 125 atoms. From the AIMD simulated structural patterns at a temperature of 500 K (see Figs. 1(d), 1(e) and S1 [38]), one sees that overall, the local bond structure remains intact. The result confirms the thermal stability of TiB_2C_2 and HfB_2C_2 at 500 K.

To investigate the in-plane stiffness of both nanosheets, we calculated the energies with different isotropic surface strains


 FIG. 2. The electronic band structures of (a) and (b) TiB_2C_2 and (c) and (d) HfB_2C_2 nanosheets.

along the a and b axes. Figure 1(f) shows the relative energy dE ($dE = E - E_0$) per unit cell as a function of isotropic surface strain $e = (A - A_0)/A_0$. We could get the surface Young's modulus according to $Y_{2D} = A_0^{-1}(\partial^2 E/\partial e^2)_{e=0}$, where A_0 is equilibrium surface area of the unit cell. $Y_{2D} = 137.8$ N/m for the TiB_2C_2 nanosheet, and $Y_{2D} = 128.9$ N/m for the HfB_2C_2 nanosheet. The in-plane Young's moduli are about 40% and 37% of that of graphene, and they exhibit high mechanical strength.

Considering the experimental feasibility of our proposed structures, they could be synthesized by controlled doping from TM borides using the molecular beam epitaxy technique as we mentioned above [20]. In addition, chemical vapor deposition (CVD) growth also offers opportunities to obtain high-quality and large-size alloyed single- or multi-layer transition metal 2D nanosheets. TiB_2C_2 and HfB_2C_2 can be grown well on specific substrates (such as Ag, Cu, Si, SiO_2 , and so on) under extreme conditions (e.g., high temperature, strong oxidizing agents, and so on). For example, Liu *et al.* reported the synthesis of $\text{Mo}_{1-x}\text{W}_x\text{S}_2$ alloys by sulfurizing as-prepared $\text{Mo}_{1-x}\text{W}_x$ thin films through the CVD process [39], and Xu *et al.* also reported the synthesis of large-area high-quality 2D ultrathin Mo_2C crystals using the CVD method [40].

B. The Dirac states in TiB_2C_2 and HfB_2C_2 nanosheets

We plotted the electronic band structure along high-symmetry points Γ - M - K - Γ as well as the three-dimensional (3D) valence and conduction band surface to analyze the

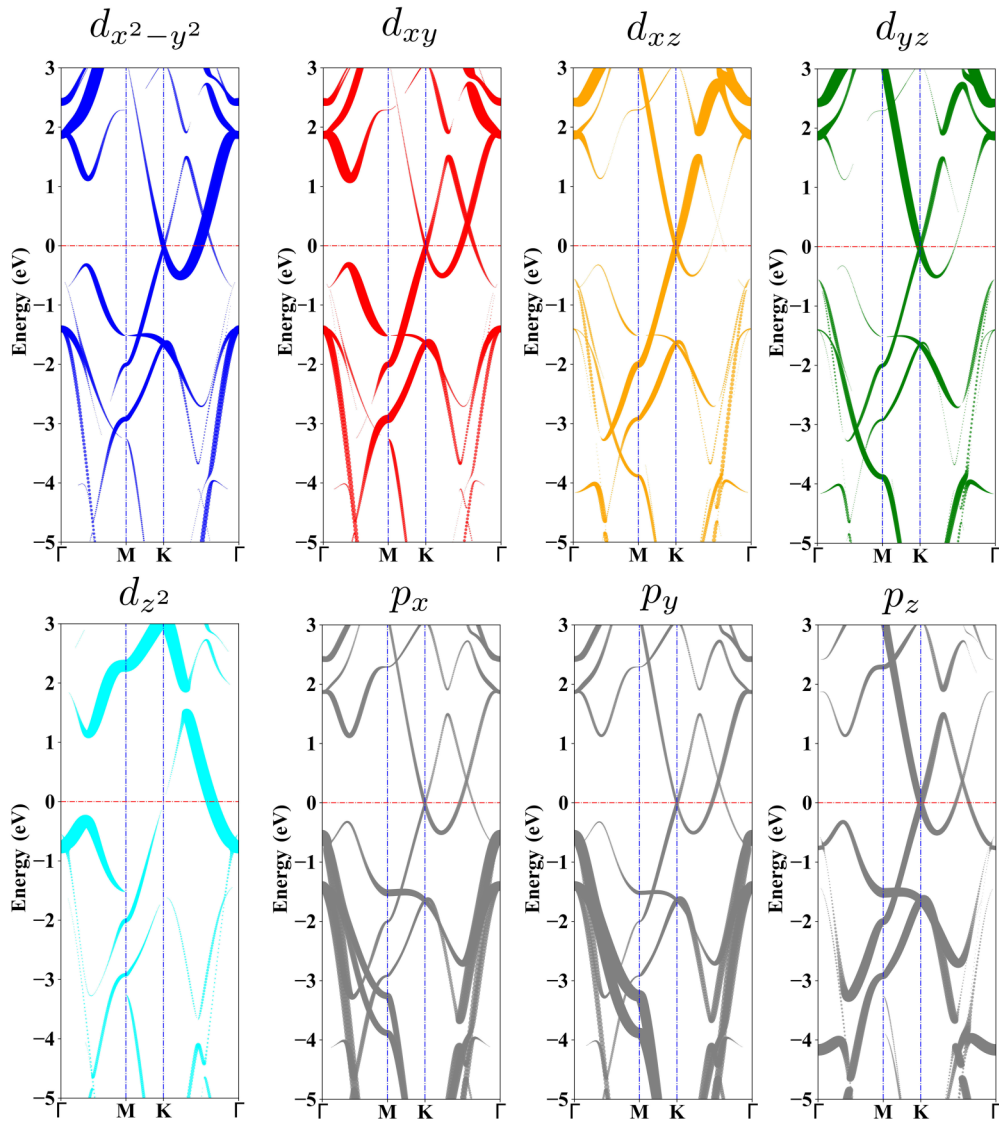


FIG. 3. The electronic band projection structures of TiB_2C_2 nanosheets.

electronic characters of TiB_2C_2 and HfB_2C_2 (see Figs. 2 and S2 [38]). There are two Dirac cones around the K point; one is at the K point, and the other is at the off-symmetry point between Γ and K , which we denote as D . Two Dirac cones are characterized with compensated electron-hole pockets.

To get further understanding of the contribution of the two Dirac cones, we plot the projected band structures of TiB_2C_2 and HfB_2C_2 nanosheets in Figs. 3 and 4, respectively. Considering the D_{3d} point group symmetry, the five d orbitals of TiB_2C_2 will split into three groups: e_1^* (d_{xz} degenerate with d_{yz}), e_1 (d_{xy} degenerate with $d_{x^2-y^2}$), and a_1^* (d_{z^2}). In Fig. 3, for p and d orbitals, the radii of the different colored lines are proportional to the corresponding orbital contribution. The result suggests that the first Dirac point at K is mainly from degenerate d_{yz} and d_{xz} as well as degenerate d_{xy} and $d_{x^2-y^2}$ of Ti atoms and p_z orbitals of boron and carbon atoms. The result implies that the four orbitals of Ti atoms mainly hybridize with p_z orbitals of boron and carbon atoms. The second Dirac

point at D , which locates along Γ to K , is mainly from the three d orbitals (d_{xy} , $d_{x^2-y^2}$, and d_{z^2}) of Ti atoms. We also made a comparison with the C p orbital and B p orbital of TiB_2C_2 (see Fig. S3 [38]); the result suggests that the p orbitals of B and C exhibit similar band dispersion, and B p orbitals contribute more states than those of C p orbitals at the K point. The electronic band character of the HfB_2C_2 nanosheet follows the same rule as that of TiB_2C_2 .

C. Robust Dirac states in the TiB_2C_2 and HfB_2C_2 nanosheets against various external strains

As we mentioned in the Introduction, the ZrB_2 nanosheet exhibits multiple Dirac states. While the one along Γ to M is sensitive to external isotropic biaxial strain, the other one along Γ to K is robust against isotropic biaxial strain. For TiB_2C_2 and HfB_2C_2 nanosheets, both Dirac cones are robust against isotropic biaxial strain as well as anisotropic strains. As shown in Fig. 5, as for the electronic structures

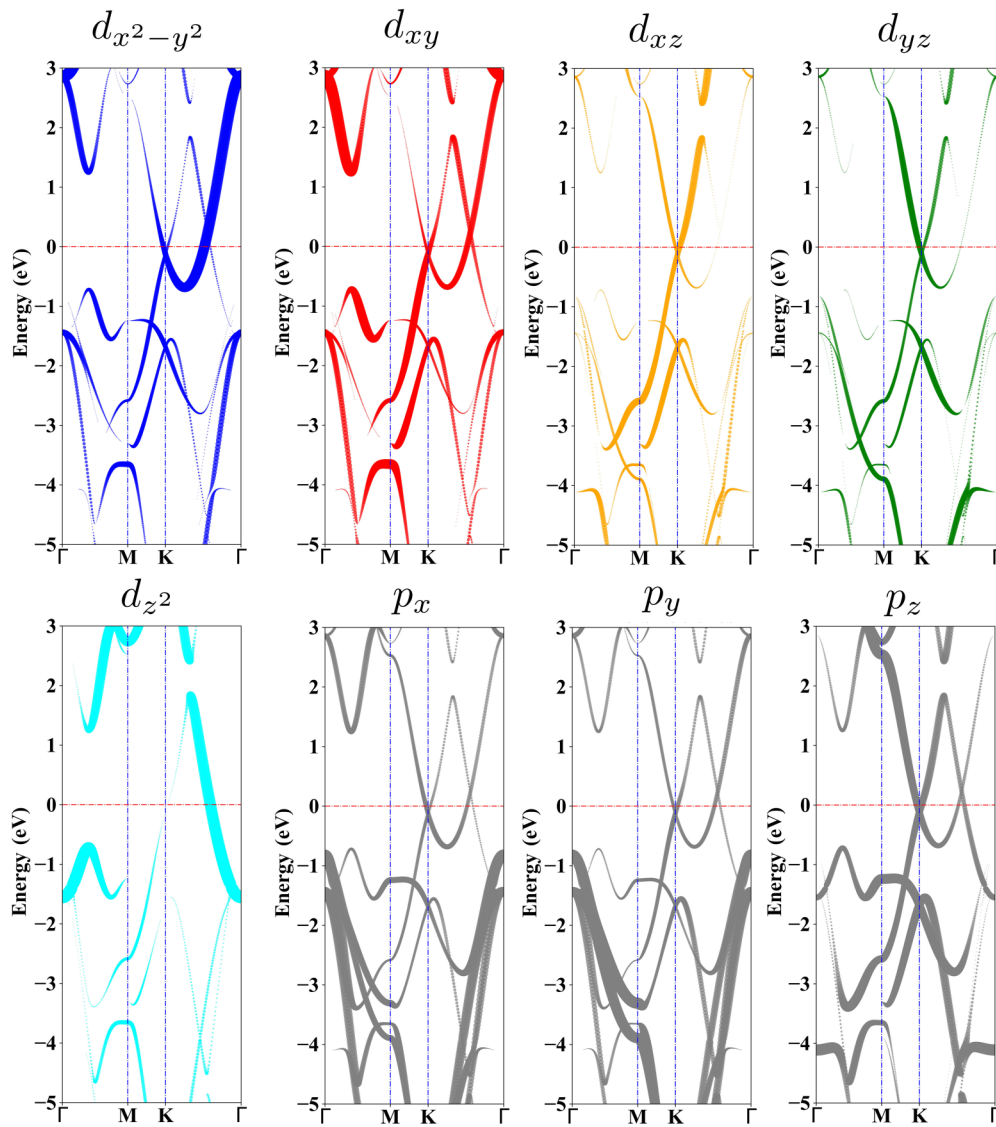


FIG. 4. The electronic band projection structures of HfB_2C_2 nanosheets.

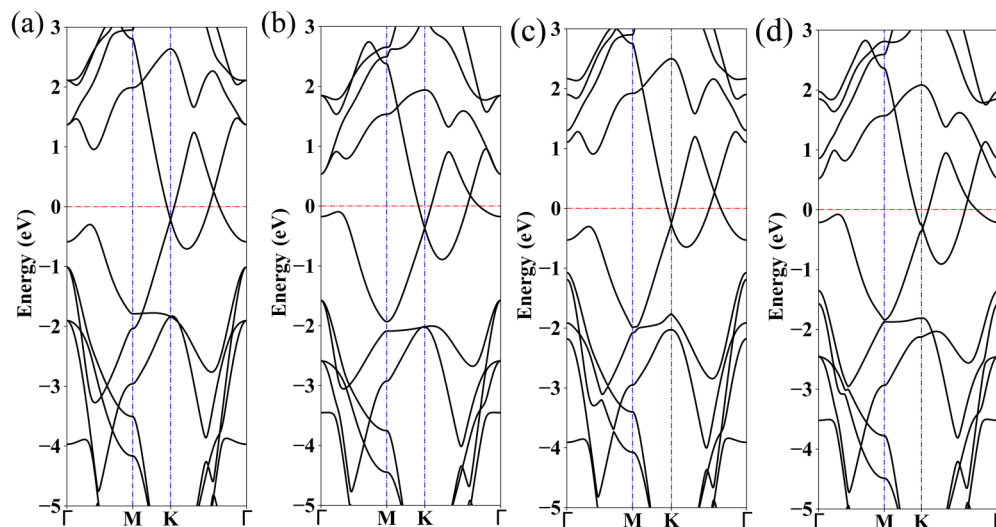


FIG. 5. The electronic band structures of TiB_2C_2 under isotropic strains of (a) -3% and (b) 3% and anisotropic strains of (c) -3% and (d) 3% .

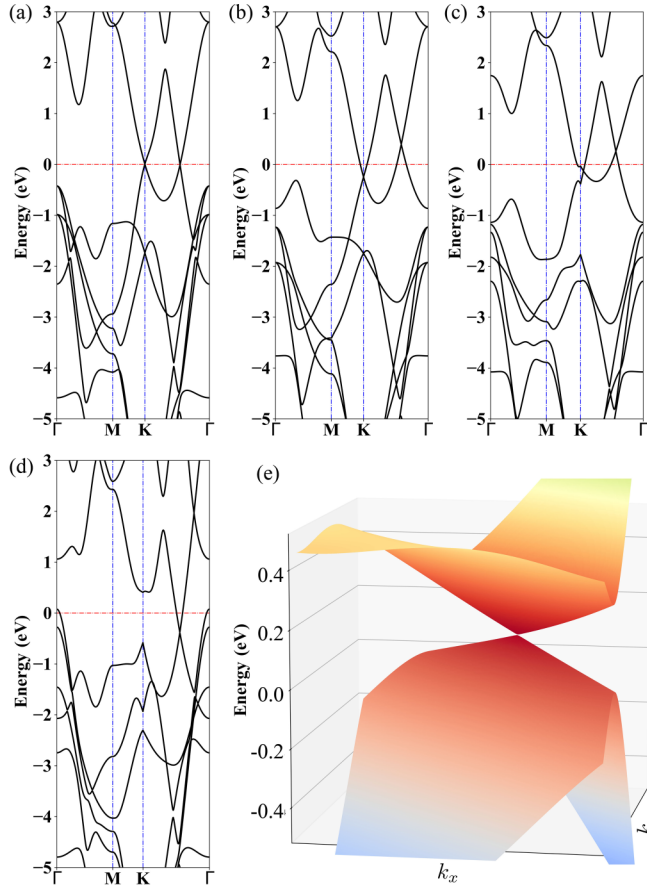


FIG. 6. The electronic band structures of HfB_2C_2 under isotropic strains of (a) -4.5% and (b) 4% and anisotropic strains of (c) -3% and (d) 3% ; 3D band structure around the K point is shown in (e) to confirm the Dirac cone shift.

under isotropic strains of -3% [see Fig. 5(a)] and 3% [see Fig. 5(b)], the result suggests that both Dirac cones at the K and D points are robust, with the one at K shifting down a bit, and the electron-hole pockets could survive the tensile strains. To further check the robustness of the Dirac cones, we further calculated anisotropic strains of -3% [see Fig. 5(c)] and 3% [see Fig. 5(d)] along the $(1 -1 0)$ direction. The result also verified the robustness even in the absence of the D_{3d} point group symmetry, which was broken by the anisotropic strains. To investigate the mechanism of Dirac evolution under anisotropic strains, we further plotted the band structure along Γ to S $(0.5 \ 0.5 \ 0.0)$; the result implies that under anisotropic strains, K is not degenerate any longer, while both of the Dirac states still remain in line with $R_a = R_b$, where R_a and R_b are reciprocal lattice vectors (see Fig. S4 [38]). The HfB_2C_2 nanosheet exhibits a similar robustness character against these external strains. Both Dirac cones also survive under isotropic

strains of -4.5% [see Fig. 6(a)] and 4% [see Fig. 6(b)] as well as anisotropic strains of $\pm 3\%$ [see Figs. 6(c) and 6(d)]. To manipulate the energy level of the Dirac cones, we found that both Dirac cones could be shifted to Fermi energy level under isotropic strains of -4.5% . In addition, the anisotropy of the Dirac cones could be obviously enhanced under external strains, which is desirable for manipulating the direction of electron propagation [41,42].

As mentioned above, the Dirac states are from the d orbitals of the TM and p orbitals of B and C atoms; the Dirac cone contribution is different from that of TiB_2 , in which the Dirac cone is mainly from d orbitals of Ti, and the Dirac cone could survive the SOC effect. However, for both the TiB_2C_2 and HfB_2C_2 nanosheets, the Dirac cones are broken under the SOC effect, especially for the $5d$ transition metal Hf. As shown in Fig. 7, the gaps are 6.6 (18.5) and 177 (30.1) meV for the Dirac cones at K (D) for the TiB_2C_2 (HfB_2C_2) nanosheet, respectively. The result suggests that when strain is -4.5% , the HfB_2C_2 nanosheet could be successfully tuned to exhibit a metal-insulator transition, which is desirable for electronic devices.

D. Multiple Dirac cones induced by the p - d electron-counting rule and bilayer stacking

As mentioned in the Introduction, there are many TM borides proposed to be Dirac materials. The result of Dirac characters in different TM borides listed in Table II suggests that, in the hexagonal boride lattice, boron atoms with three coordinates need four valence electrons to stabilize the lattice. For example, for B_2S [43] and B_2Se [44], each S or Se atom provides two p electrons to B_2 components with a covalent bond property. For the TM borides, a similar rule dominates the lattice stability, which we named the p - d electron-counting rule for the hexagonal TM boride lattice. For TiB_2 , each Ti ($4s^2 3d^2$) contributes two electrons to the B_2 honeycomb to stabilize the lattice. This rule is obviously consistent with other TM borides in Table II, including our previously proposed ZrB_2C_2 [45].

Besides the mechanism of lattice stability, another phenomenon implies that the multiple Dirac cone states (at K and off-symmetry D) are prone to appear in bilayer nanosheets. To investigate the evolution of the band dispersion in TB_2C_2 , we calculated the electronic band of eight structures: only the Ti atom in the triangular unit cell with the lattice parameter of the TiB_2C_2 nanosheet, only the B-C bilayer in the lattice (in the absence of Ti in TiB_2C_2), and the TiB_2C_2 multiple Dirac cone nanosheet with the evolution of distance between the TM and BC honeycomb (see Fig. 8). The thickness c (perpendicular to the plane of the nanosheet) increasing from $1.3c_0$ to $2.5c_0$, where c_0 is the thickness of the ground state of TiB_2C_2 nanosheet, the result shown in Fig. 8 suggests that,

TABLE II. Dirac character in different 2D borides nanosheets: Dirac point position (DP) associated with symmetry (SYM).

| | $\text{B}_2\text{S}, \text{B}_2\text{Se}$ | TiB_2 | ZrB_2 | FeB_2 | TMB_4 ($T = \text{Cr}, \text{Mo}, \text{W}$) | $\text{TB}_2\text{C}_2/\text{TB}_2\text{Si}_2$ ($T = \text{Ti}, \text{Zr}, \text{Hf}$) |
|-----|---|----------------|------------------------------|----------------|--|---|
| SYM | D_{2h} | C_{6v} | C_{6v} | C_{6v} | D_{6d} | D_{3d} |
| DP | Γ - Y | Γ - K | Γ - K, Γ - M | K | Γ - K, K | Γ - K, K |

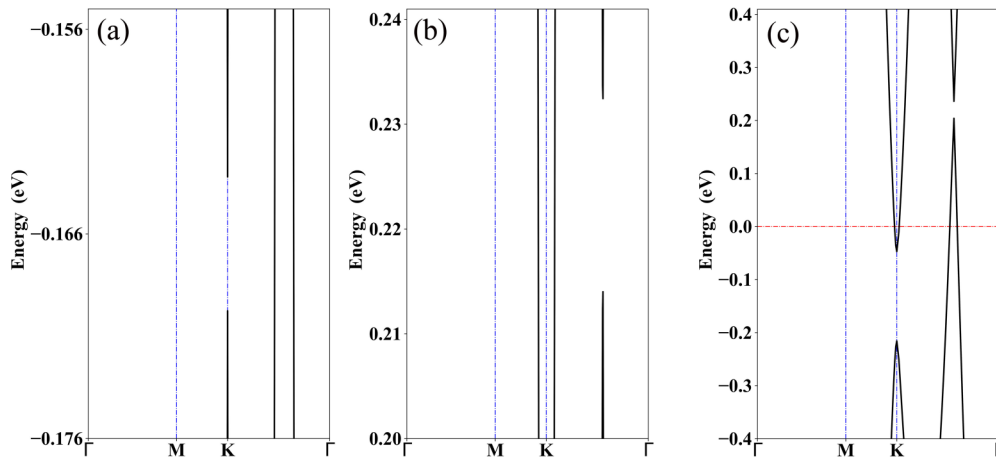


FIG. 7. The electronic band structures of (a) and (b) TiB_2C_2 and (c) HfB_2C_2 with the SOC effect.

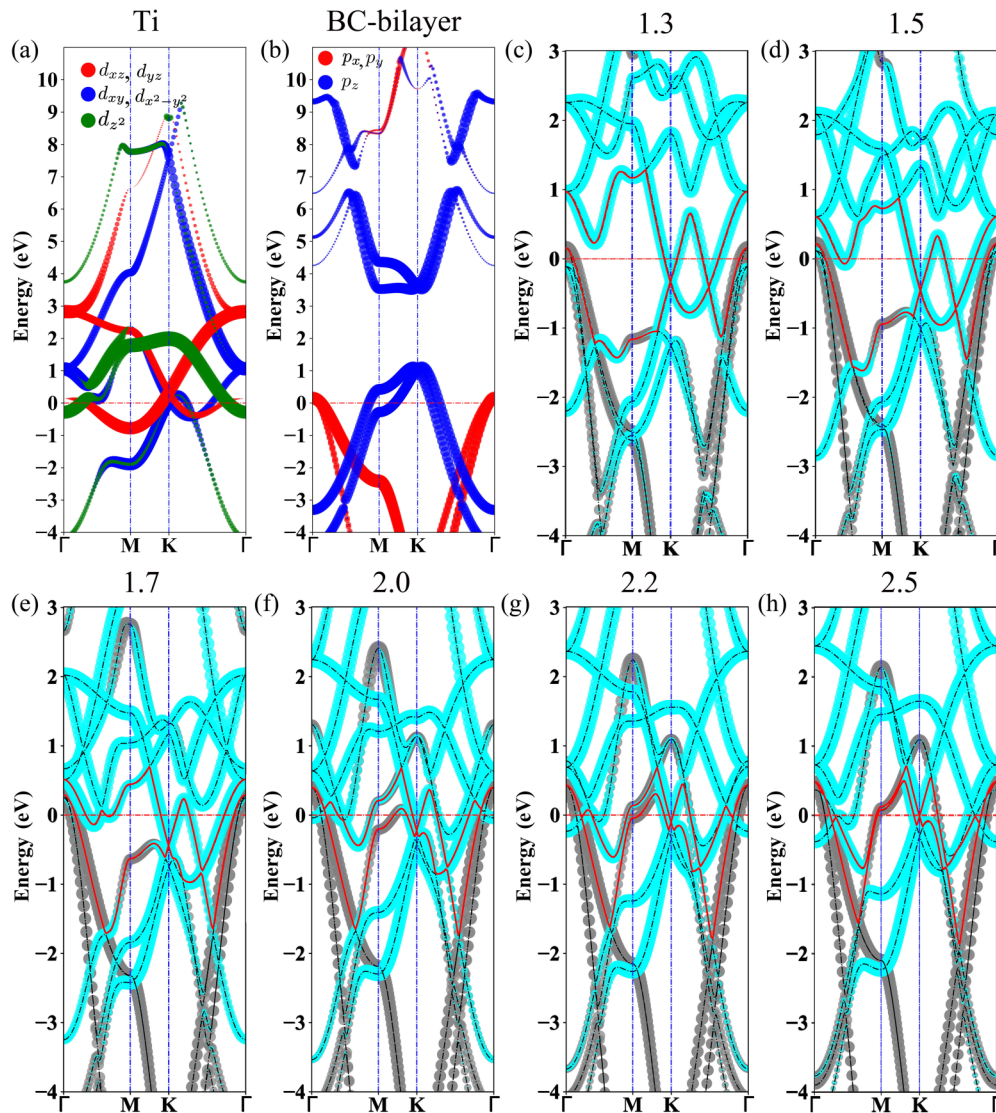


FIG. 8. Electronic band structures: (a) only Ti in the hexagonal lattice, (b) only the B-C bilayer in the hexagonal lattice, and (c)–(h) TiB_2C_2 nanosheet with the lattice perpendicular to the plane increased by 30%, 50%, 70%, 100%, 120%, 150%, respectively. The states in cyan and gray are from Ti d and BC p orbitals, and the two bands which form Dirac cones we marked by a red line to follow the band evolution.

TABLE III. On-site energy (eV) evolution for d orbitals from the triangular Ti lattice to TiB_2 and TiB_2C_2 nanosheets.

| | d_{z^2} | d_{xz}, d_{yz} | $d_{xy}, d_{x^2-y^2}$ |
|--------------------------|-----------|------------------|-----------------------|
| Ti | 1.24 | 1.22 | 1.10 |
| TiB_2 | 0.99 | 0.67 | 0.88 |
| TiB_2C_2 | 0.72 | 1.90 | 1.11 |

with the Ti and BC layer interaction evolution from $2.5c_0$ to c_0 (see Figs. 8 and 2), the ninth and tenth bands (red line) form two Dirac cones with the one at D shift upward. Compared with TiB_2 , whose states shift upward away from the Fermi energy at K and end up with one Dirac cone at the off-symmetry point, the bilayer BC interacts with Ti in inversion symmetry, and it could obviously change the on-site energy of Ti d orbitals with a crystal split sequence different from that of TiB_2 .

To investigate the origin of multiple Dirac states in these hexagonal TM borides, we further fitted the tight-binding Hamiltonian with maximally localized Wannier functions [46] to the electronic band structure calculated by DFT. Table III lists the on-site energy of five d orbitals of Ti for the Ti triangular lattice, TiB_2 nanosheet, and TiB_2C_2 nanosheet. The schematic diagram of the d orbital energy split evolution is shown in Fig. 9: The crystal field split in the Ti triangular lattice is in the D_{6h} symmetry, and e_1 is below the other two groups, between which the split is only 0.02 eV. The d orbital split for TiB_2 increased, and the energy sequence between e_1 and e_1^* reversed under C_{6v} symmetry of C_{6v} . For TiB_2C_2 , the symmetry is D_{3d} , and the crystal splitting increases more strongly than that of TiB_2 , and the energy split increases by 0.37 eV compared with that of the Ti triangular lattice. As shown in Fig. 3, the Dirac point at D is mainly from e_1 and a_1^* , the D point is obviously shifted up compared with that of TiB_2 , and this shift dominates the second Dirac cone. The result suggests that for 2D TM borides, the p - d electron-counting rule and crystal field split induced by inversion-symmetric bilayer stacking are crucial for the emergence of multiple Dirac cones.

To verify our opinion, we further calculated the phonon and electronic band structures of TB_2Si_2 ($T = \text{Ti}, \text{Zr}$ and Hf), all of which have been proved to be stable bilayer nanosheets

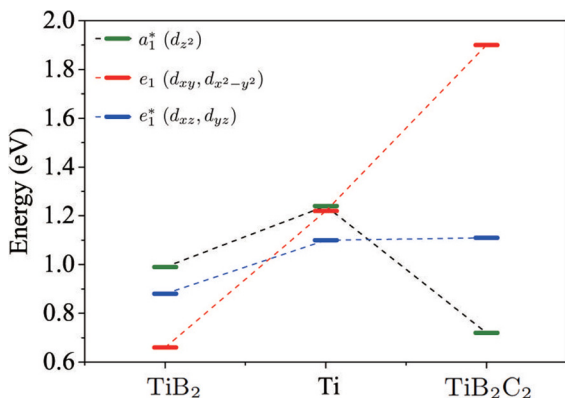


FIG. 9. Crystal field split for d orbitals in different lattices.

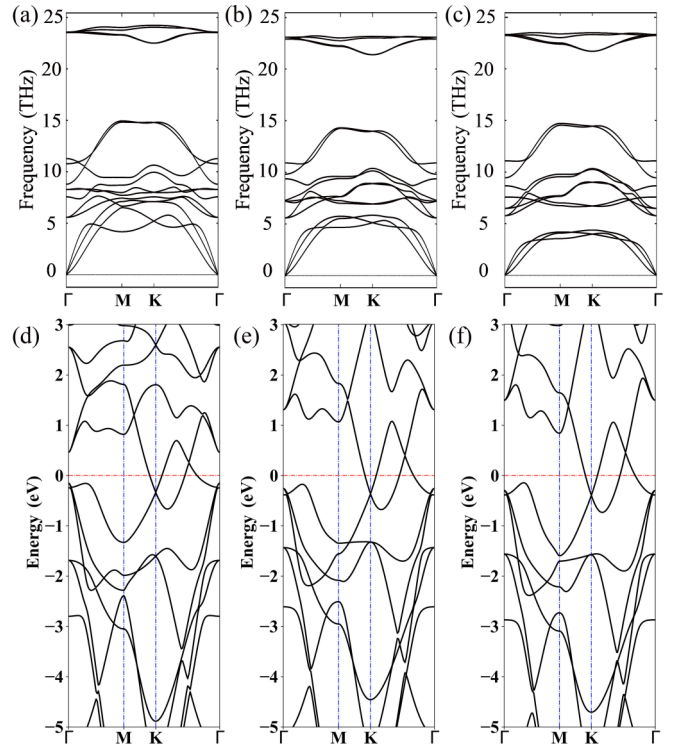


FIG. 10. Phonon and electronic band structures of (a) and (d) TiB_2Si_2 , (b) and (e) ZrB_2Si_2 , and (c) and (f) HfB_2Si_2 , respectively.

exhibiting multiple Dirac cones (see Fig. 10); the structure and structure parameters are shown in Fig. S5 and Table S1 [38].

IV. CONCLUSION

In summary, we predicted two different 2D TiB_2C_2 and HfB_2C_2 nanosheets, whose stabilities are verified by total structural atomic relaxations, the phonon dispersion calculations, and the AIMD calculations, which reveal that both nanosheets could hold up to the temperature of 500 K. The planar Young's moduli are 137.8 N/m for TiB_2C_2 and 128.9 N/m for HfB_2C_2 , which are about 40% and 37% of that of graphene, respectively. Both nanosheets exhibit 12 Dirac cones in their first BZ. All of the Dirac cones are robust under different types of external strains; the robustness of both Dirac cones is a promising property for electronic devices for its high electron-mobility and low-power dissipation. And the Dirac cones could be tuned by external strain to be anisotropic, which is desirable for manipulating the direction of electron propagation. We also proposed that for transition metal borides, multiple Dirac cones could be induced by the combination of the p - d electron-counting rule and bilayer stacking. We further proved that TB_2Si_2 ($T = \text{Ti}, \text{Zr}, \text{Hf}$) nanosheets are mechanically stable using this mechanism, which could also be used to predict other multiple Dirac state 2D materials.

ACKNOWLEDGMENTS

This work was supported by the NSFC (Grant No. 11674185), the Natural Science Foundation of Fujian (Grant

No. 2019J01764), and the Natural Science Foundation of Ningbo (Grant No. 2018A610007). The numerical calculations were carried out at the High Performance Computing

Center (HPCC) of Nanjing University and Fujian Provincial Key Laboratory of Information Processing and Intelligent Control, Minjiang University.

- [1] K. S. Novoselov, A. K. Geim, S. V. Morozov, D. Jiang, Y. Zhang, S. V. Dubonos, I. V. Grigorieva, and A. A. Firsov, *Science* **306**, 666 (2004).
- [2] P. Vogt, P. De Padova, C. Quaresima, J. Avila, E. Frantzeskakis, M. C. Asensio, A. Resta, B. Ealet, and G. Le Lay, *Phys. Rev. Lett.* **108**, 155501 (2012).
- [3] M. E. Dvila, L. Xian, S. Cahangirov, A. Rubio, and G. Le Lay, *New J. Phys.* **16**, 095002 (2014).
- [4] F. F. Zhu, W. J. Chen, Y. Xu, C. L. Gao, D. D. Guan, C. H. Liu, D. Qian, S. C. Zhang, and J. F. Jia, *Nat. Mater.* **14**, 1020 (2015).
- [5] M. H. Evans, J. D. Joannopoulos, and S. T. Pantelides, *Phys. Rev. B* **72**, 045434 (2005).
- [6] H. Tang and S. Ismail-Beigi, *Phys. Rev. B* **82**, 115412 (2010).
- [7] H. Tang and S. Ismail-Beigi, *Phys. Rev. Lett.* **99**, 115501 (2007).
- [8] H. Liu, J. Gao, and J. Zhao, *Sci. Rep.* **3**, 3238 (2013).
- [9] L. Z. Zhang, Z. F. Wang, S. X. Du, H. J. Gao, and F. Liu, *Phys. Rev. B* **90**, 161402(R) (2014).
- [10] A. Lopez-Bezanilla, *Phys. Rev. Materials* **2**, 011002(R) (2018).
- [11] Y. An, J. Jiao, Y. Hou, H. Wang, R. Wu, C. Liu, X. Chen, T. Wang, and K. Wang, *J. Phys.: Condens. Matter* **31**, 065301 (2019).
- [12] Z. Liu, P. Wang, Q. Cui, G. Yang, S. Jin, and K. Xiong, *RSC Adv.* **9**, 2740 (2019).
- [13] H. Zhang, Y. Li, J. Hou, A. Du, and Z. Chen, *Nano Lett.* **16**, 6124 (2016).
- [14] H. Zhang, Y. Li, J. Hou, K. Tu, and Z. Chen, *J. Am. Chem. Soc.* **138**, 5644 (2016).
- [15] X.-J. Weng, X.-L. He, J.-Y. Hou, C.-M. Hao, X. Dong, G. Gao, Y. Tian, B. Xu, and X.-F. Zhou, *Phys. Rev. Materials* **4**, 074010 (2020).
- [16] A. Lopez-Bezanilla, *2D Mater.* **5**, 035041 (2018).
- [17] S. Y. Xie, X. B. Li, W. Q. Tian, N. K. Chen, X. L. Zhang, Y. Wang, S. Zhang, and H. B. Sun, *Phys. Rev. B* **90**, 035447 (2014).
- [18] C. Zhang, Y. Jiao, F. Ma, S. Bottle, M. Zhao, Z. Chen, and A. Du, *Phys. Chem. Chem. Phys.* **19**, 5449 (2017).
- [19] A. Lopez-Bezanilla, *J. Phys.: Mater.* **3**, 024002 (2020).
- [20] C. Cepek, R. Macovez, M. San Corti, L. Prtaccia, R. Larciprete, S. Lizzt, and A. Goldoni, *Appl. Phys. Lett.* **85**, 976 (2004).
- [21] G. Hilz and H. Holleck, *Int. J. Refract. Met. Hard Mater.* **14**, 97 (1996).
- [22] A. S. Pereira, C. A. Perotoni, J. A. H. da Jornada, J. M. Léger, and J. Haines, *J. Phys.: Condens. Matter* **14**, 10615 (2002).
- [23] V. V. Ivanovskaya, A. N. Enyashin, and A. L. Ivanovskii, *Inorg. Mater.* **40**, 134 (2004).
- [24] X. Feng, C. Yue, Z. Song, Q. S. Wu, and B. Wen, *Phys. Rev. Materials* **2**, 014202 (2018).
- [25] T. Lundström, B. Lönnberg, and I. Westman, *J. Less-Common Met.* **96**, 229 (1984).
- [26] W. G. Fahrenholtz, G. E. Hilmas, I. G. Talmy, and J. A. Zaykoski, *J. Am. Ceram. Soc.* **90**, 1347 (2007).
- [27] S. Otani, T. Aizawa, and N. Kieda, *J. Alloys Compd.* **475**, 273 (2009).
- [28] L. T. Alameda, P. Moradifar, Z. P. Metzger, N. Alem, and R. E. Schaak, *J. Am. Chem. Soc.* **140**, 8833 (2018).
- [29] M. Naguib, M. Kurtoglu, V. Presser, J. Lu, J. Niu, M. Heon, L. Hultman, Y. Gogotsi, and M. W. Barsoum, *Adv. Mater.* **23**, 4248 (2011).
- [30] M. Naguib, V. N. Mochalin, M. W. Barsoum, and Y. Gogotsi, *Adv. Mater.* **26**, 992 (2014).
- [31] J. P. Perdew, K. Burke, and M. Ernzerhof, *Phys. Rev. Lett.* **77**, 3865 (1996).
- [32] G. Kresse and J. Hafner, *Phys. Rev. B* **47**, 558 (1993).
- [33] A. Togo and I. Tanaka, *Scr. Mater.* **108**, 1 (2015).
- [34] S. Baroni, S. D. Gironcoli, A. D. Corso, and P. Giannozzi, *Rev. Mod. Phys.* **73**, 515 (2001).
- [35] G. J. Martyna, M. L. Klein, and M. Tuckerman, *J. Chem. Phys.* **97**, 2635 (1992).
- [36] H. J. Monkhorst and J. D. Pack, *Phys. Rev. B* **13**, 5188 (1976).
- [37] P. E. Blöchl, O. Jepsen, and O. K. Andersen, *Phys. Rev. B* **49**, 16223 (1994).
- [38] See Supplemental Material at <http://link.aps.org/supplemental/10.1103/PhysRevB.102.165404> for the geometric structure of the 500 K molecular dynamics results (Fig. S1), a contour plot of six pairs of Dirac cones and the zoomed-in electronic band structure (Fig. S2), the electronic band projections of p orbitals from C and B atoms (Fig. S3), electronic band structures along Γ (000) to S (0.5 0.5 0) (Fig. S4), geometric structures (Fig. S5), and structural parameters (Table S1) of TB_2Si_2 ($T = \text{Ti, Zr, Hf}$).
- [39] H. Liu, K. K. A. Antwi, S. Chua, and D. Chi, *Nanoscale* **6**, 624 (2014).
- [40] C. Xu, L. Wang, Z. Liu, L. Chen, J. Guo, N. Kang, X. Ma, H. Cheng, and W. Ren, *Nat. Mater.* **14**, 1135 (2015).
- [41] C. H. Park, L. Yang, Y. W. Son, M. L. Cohen, and S. G. Louie, *Nat. Phys.* **4**, 213 (2008).
- [42] Z. F. Wang and F. Liu, *ACS Nano* **4**, 2459 (2010).
- [43] Y. Zhao, X. Li, J. Liu, C. Zhang, and Q. Wang, *J. Phys. Chem. Lett.* **9**, 1815 (2018).
- [44] J. Lyu, W. Ji, S. Zhang, C. Zhang, and P. Wang, *J. Phys. Chem. C* **124**, 7558 (2020).
- [45] B. Zhang, Y. Li, C. Zhang, and J. Wang, *Phys. Chem. Chem. Phys.* **21**, 24212 (2019).
- [46] A. A. Mostofi, J. R. Yates, G. Pizzi, Y. S. Lee, I. Souza, D. Vanderbilt, and N. Marzari, *Comput. Phys. Commun.* **185**, 2309 (2014).